Journal Pre-proof

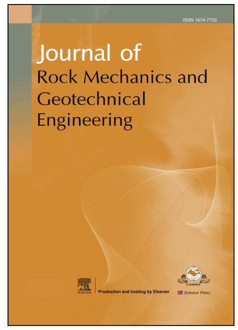

Coupled effects of heterogeneity and propagation regime on hydraulic fracture morphology

Mengli Li, Mengyi Li, Jidong Zhao, Fengshou Zhang, Egor Dontsov, Tuo Wang

PII: S1674-7755(26)00367-7

DOI: https://doi.org/10.1016/j.jrmge.2026.03.055

Reference: JRMGE 2712

To appear in: *Journal of Rock Mechanics and Geotechnical Engineering*

Received Date: 23 November 2025

Revised Date: 16 February 2026

Accepted Date: 10 March 2026

Please cite this article as: Li M, Li M, Zhao J, Zhang F, Dontsov E, Wang T, Coupled effects of heterogeneity and propagation regime on hydraulic fracture morphology, *Journal of Rock Mechanics and Geotechnical Engineering*, https://doi.org/10.1016/j.jrmge.2026.03.055.

This is a PDF of an article that has undergone enhancements after acceptance, such as the addition of a cover page and metadata, and formatting for readability. This version will undergo additional copyediting, typesetting and review before it is published in its final form. As such, this version is no longer the Accepted Manuscript, but it is not yet the definitive Version of Record; we are providing this early version to give early visibility of the article. Please note that Elsevier's sharing policy for the Published Journal Article applies to this version, see: https://www.elsevier.com/about/policies-and-standards/sharing#4-published-journal-article. Please also note that, during the production process, errors may be discovered which could affect the content, and all legal disclaimers that apply to the journal pertain.

© 2026 Institute of Rock and Soil Mechanics, Chinese Academy of Sciences. Published by Elsevier B.V.

Journal Pre-proof

Coupled effects of heterogeneity and propagation regime on hydraulic fracture morphology

Mengli Li[1], Mengyi Li[2], Jidong Zhao[1], Fengshou Zhang[3, *], Egor Dontsov[4], Tuo Wang[5]

[1] Department of Civil and Environmental Engineering, The Hong Kong University of Science and Technology, Hong Kong, 999077, China

[2] School of Civil Engineering, Wuhan University, Wuhan, 430072, China

[3] Department of Geotechnical Engineering, Tongji University, Shanghai, 200092, China

[4] ResFrac Corporation, 555 Bryant Street, #185 Palo Alto, CA 94301, USA

[5] Department of Civil and Environmental Engineering, The Hong Kong Polytechnic University, Hong Kong, 999077, China

*Corresponding author. E-mail address: fengshou.zhang@tongji.edu.cn

Abstract: Fluid-driven fracturing is fundamental to geophysical processes (e.g. fluid-induced seismicity) and engineered applications such as geothermal energy extraction. This study investigates the coupled influence of rock heterogeneity and fracture propagation regime on hydraulic fracture growth. Using a fully coupled discrete element-pore network model, we simulate fracture propagation driven by both Newtonian and shear-thinning power-law fluids. Rock heterogeneity is explicitly represented by a Weibull distribution of mechanical properties, allowing fractures to initiate and propagate without predefined paths. Model validation shows excellent agreement with classical Khristianovic–Geertsma–de Klerk (KGD) solutions across viscosity- and toughness-dominated regimes. Our results demonstrate that heterogeneity strongly influences fracture morphology. In highly heterogeneous rocks, viscosity-dominated propagation creates broad process zones with distributed microcracking and high orthogonal roughness. In contrast, toughness-dominated propagation leads to localized stress perturbations, forming tortuous and asymmetric fractures. Shear-thinning fluids reduce the morphological contrast between regimes by decreasing the effective near-tip viscosity, while time-evolving propagation behavior further moderates regime-dependent differences. Ultimately, fracture complexity is governed by the interplay between fluid rheology and material heterogeneity. These findings provide critical insights for optimizing fluid selection and injection parameters to achieve desired fracture complexity and containment in heterogeneous reservoirs.

Keywords: Discrete element method (DEM); Hydraulic fracturing; Fracture propagation regimes; Heterogeneity; Fracture morphology

1. Introduction

Fluid-driven fracture processes are fundamental to both geophysical phenomena, such as magmatic dike propagation, and engineered systems, including energy extraction from low-permeability hot dry rock (HDR) (Economides and Nolte, 2000). Predicting and controlling fracture geometry is challenging due to the coupled effects of fluid rheology, injection parameters, and rock heterogeneity, with implications for induced seismicity and fracture network efficiency. Enhanced geothermal systems (EGS), exemplified by over 60 projects worldwide including the Gonghe Basin in China (Zhang et al., 2024), rely on hydraulic fracturing to overcome low HDR permeability and establish conductive networks for efficient heat exchange. Similar principles apply to stimulation in tight petroleum formations, where heterogeneity strongly influences fracture connectivity and morphology (Guo et al., 2018; Wang and Li, 2025). Understanding these processes provides a mechanistic basis for optimizing hydraulic stimulation in engineered reservoirs and interpreting natural fracture systems.

Hydraulic fracturing exemplifies a multiphysics challenge where rock deformation, viscous fluid flow within fractures, leak-off into the porous matrix, and fracture propagation are strongly coupled (Lecampion et al., 2018; Yang et al., 2024). These interactions occur across multiple spatial and temporal scales, ranging from micrometer-scale asperity failure to kilometer-scale fracture networks, and from rapid fracture tip advancement to slower leak-off and reservoir-scale pressure diffusion (Zhang et al., 2019a). Within this multiscale setting, two sets of competing mechanisms govern the near-tip asymptotics: energy dissipation mechanisms (rock fracturing and viscous flow) and fluid balance mechanisms (leak-off and fluid storage within the fracture) (Garagash et al., 2011; Detournay, 2016; Liu et al., 2025). Their relative dominance depends on injection rate, fluid viscosity, rock mechanical properties, and formation permeability, giving rise to distinct propagation regimes (toughness-dominated, viscosity-dominated, leak-off-dominated, or transitional) within a dimensionless parametric space (Hu and Garagash, 2010; Detournay, 2016). While this theoretical framework provides a rigorous baseline for idealized homogeneous media, natural formations are inherently heterogeneous and anisotropic. Heterogeneity occurs across scales, from mineral composition and pore structure at the grain scale, to natural fractures at the core scale, and stratification or faults at the field scale (Zhang et al., 2019b; Wang et al., 2025b). This multiscale complexity significantly alters the coupled hydromechanical response, often producing asymmetric fracture growth and intricate fracture networks (Zhuang and Zang, 2021; Wu et al., 2022). Understanding how heterogeneity influences fracture propagation is therefore central to the present investigation.

Granite, a representative crystalline rock and typical host formation for HDR-based EGS projects, consists mainly of quartz, feldspar, and mica, with pronounced heterogeneity in grain size, shape, and orientation. This polymineralic mesostructure governs stress redistribution and the competition between intergranular and intragranular fracture propagation (Zhuang et al., 2020; Wang et al., 2025b). Laboratory studies on Pocheon granite reveal frequent intragranular propagation within quartz due to its relatively low tensile strength, with fragmented grains showing strong interactions between advancing fractures and pre-existing microcracks (Zang et al., 2019). Coarser and more uniformly distributed grains tend to promote fracture linkage along grain boundaries and increase tortuosity, a behavior commonly associated with shear-dominated propagation (Ishida et al., 2000). Yet, under low-permeability conditions, recent observations suggest a shift toward tensile fracturing (Zhang et al., 2025). These findings underscore the complex role of grain-scale features in governing hydraulic fracture behavior.

The effects of rock mesostructure on fracture propagation can be incorporated into numerical models using either explicit or implicit approaches. Explicit approaches reconstruct mineral grain geometries, typically via Voronoi tessellations or digital image processing, and have been widely applied to study the mechanical response and microcrack development of crystalline rocks (Lan et al., 2010; Potyondy, 2010). They have also been extended to simulate fluid-driven fracture propagation at the grain scale (Kong et al., 2024). However, because the assigned intergranular strength is typically lower, explicit models often over-predict boundary-controlled propagation relative to experimental observations of intragranular fracturing (Li et al., 2020; Zhuang et al., 2020). Implicit approaches, by contrast, assign spatially varying mechanical properties (e.g. tensile strength, elastic modulus) based on probability distributions such as the Weibull function, effectively capturing the aggregate effects of heterogeneity with high computational efficiency. Prior studies have shown that such probabilistic heterogeneity can dictate the paths and modes of fracture initiation and propagation in stiff geomaterials, leading to behaviors that deviate from linear elastic fracture mechanics (LEFM) predictions (Ouchi et al., 2017; Wu et al., 2022). Nevertheless, the role of strength heterogeneity in the hydraulic fracturing process remains poorly quantified. Building on this framework, the present study adopts an implicit representation of rock property variability to investigate the evolution of hydraulic fractures under viscosity- and toughness-dominated regimes.

In deep geothermal reservoirs, elevated in situ stress and the widespread use of low-viscosity fluids (e.g. water or slickwater) often drive fracture propagation into a toughness-dominated regime (Tanné et al., 2022). In this regime, fracture tips are highly sensitive to local heterogeneities, frequently leading to asymmetric propagation. Such asymmetry has been reported in laboratory experiments (Bunger and Detournay, 2008), numerical simulations (Huang et al., 2019; Li et al., 2025b), and field observations (Fischer et al., 2008). For instance, during the Gonghe HDR project, vertical well GH-01 exhibited stronger connectivity with directional well GH-02 than with GH-03, indicative of asymmetric fracture growth in situ (Zhang et al., 2024). However, how grain-scale heterogeneity influences fracture geometry across contrasting propagation regimes (viscosity- vs. toughness-dominated) remains underexplored. Specifically, the extent to which material variability drives complex behaviors, such as branching intensity, within these regimes lacks systematic characterization. To address this, we employ a numerical model with Weibull-distributed properties to simulate fracture propagation driven by both Newtonian and power-law fluids, thereby quantifying the effects of rock mesostructural variability on fracture evolution.

In this study, a fully coupled hydromechanical discrete element model (DEM) (Cundall, 1971) is developed to investigate regime-dependent fracturing behaviors at the mesoscale, with particular emphasis on fracture energy dissipation and the evolving complexity of fracture networks. The analysis is performed within a dimensionless parametric space to reduce complexity of the problem. The remainder of this paper is organized as follows: Section 2 introduces the numerical formulation, including the discrete element method with Weibull-distributed properties and the fluid-solid coupling scheme. Section 3 presents model verification against the Khristianovic–Geertsma–de Klerk (KGD) benchmark solution (Dontsov, 2017). Section 4 explores the effects of heterogeneity and propagation regimes, while Section 5 further discusses the complex behavior of hydraulic fractures in heterogeneous rock. This study highlights the interplay between energy dissipation and heterogeneity in governing hydraulic fracture propagation, offering insights for optimizing fracturing strategies and enhancing the viability of EGS projects.

2. Numerical formulation

2.1 Representation of heterogeneity in DEM

In this study, the rock mass is represented using DEM, where the material is idealized as an assembly of rigid particles whose translational and rotational motions follow Newton's laws under the action of contact forces and moments (Cundall, 1971). The explicit time-integration scheme allows fracture initiation, propagation, and coalescence to emerge directly from the contact-scale mechanical response without predefining fracture paths. Interactions between neighboring particles are defined by contact models that capture both the elastic deformation prior to failure and the subsequent post-failure behavior.

To approximate the cohesive behavior of intact rock prior to crack initiation, the parallel bond model (Potyondy and Cundall, 2004) is adopted (Fig. 1a). In this formulation, each bonded contact transmits not only normal and shear forces but also bending and twisting moments, thereby mimicking finite-sized cementitious bridges that link mineral grains. The bonded interaction is governed by prescribed normal and shear stiffnesses, and bond breakage is determined by stress-based criteria: tensile failure occurs when the normal stress within the bond exceeds its tensile strength, while shear failure is triggered when the shear stress surpasses the assigned shear strength. Once breakage occurs, the parallel bond is irreversibly removed, and the contact reverts to a purely frictional interaction, thereby enabling a natural transition from intact to fractured states within the micromechanical framework.

In many DEM studies, bonded contact properties such as tensile strength, cohesion, and stiffness are assigned as uniform values. This simplification neglects inherent microscale heterogeneity arising from mineralogical variability and microstructural imperfections. To capture this variability, the present study assigns mesoscale mechanical properties according to a two-parameter Weibull distribution, which has been shown to describe the statistical variability of rock failure strength more accurately than Gaussian distributions (Liu et al., 2004). The probability density function is given by

$$f(\lambda) = \begin{cases} \frac{m}{\lambda_0}\left(\frac{\lambda-\lambda_{\mathrm{u}}}{\lambda_0}\right)^{m-1} \mathrm{e}^{-\left(\frac{\lambda-\lambda_{\mathrm{u}}}{\lambda_0}\right)^m} & (\lambda \geq \lambda_{\mathrm{u}}) \\ 0 & (\lambda < \lambda_{\mathrm{u}}) \end{cases} \quad (1)$$

where λ denotes the property of interest (i.e. tensile strength, cohesion and elastic modules in this study), λ_0 is the scale parameter, λ_{u} is the lower bound (commonly zero for brittle rocks), and m is the shape parameter controlling the degree of heterogeneity. Larger m values yield narrower distributions with lower variance, corresponding to greater homogeneity, whereas smaller m values reflect higher variability. The mean value $E(\lambda)$ approaches λ_0 when m is large, while the normalized deviation provides an alternative dimensionless measure of heterogeneity (Chen and Wang, 2017; Chen et al., 2020):

$$h = \frac{\sqrt{\Gamma(1+2/m)-[\Gamma(1+1/m)]^2}}{\Gamma(1+1/m)} \quad (2)$$

where $D(\lambda)$ represents the variance of λ, and Γ is the gamma function. $h \to 0$ indicates homogeneous conditions, while larger h values signify stronger heterogeneity (Fig. 1b).

Weibull-distributed random values can be generated using the inverse transform sampling method. For a uniform random variable $U \sim U(0,1)$, the transformation produces the desired distribution (assuming $\lambda_{\mathrm{u}} = 0$):

$$\lambda = \lambda_0(-\ln U)^{1/m} \quad (3)$$

Experimental determination of Weibull parameters is typically performed by fitting mechanical test data via least-squares regression (Liu et al., 2004). Previous studies highlight the scale- and material-dependence of these parameters. For instance, Pan et al. (2020) estimated m from the ratio of peak strain to the strain at unstable crack growth onset, obtaining values below 2 for highly heterogeneous cement-based rock analogs. At the mesoscale, Li et al. (2023) measured intergranular tensile strengths in Changsha granite, reporting m values between 6 and 10. Similarly, Wang et al. (2023) demonstrated that m varies across lithologies and scales. In this study, to maintain mechanical consistency, the same homogeneity index m is applied uniformly to the tensile strength, cohesion, and Young's modulus of the elements. To capture the full spectrum of heterogeneity observed in the experiments, representative values of $m = 2, 3, 5, 15$ are selected. These values cover the transition from strongly heterogeneous conditions ($h = 0.52$ for $m = 2$) to quasi-homogeneous conditions ($h = 0.08$ for $m = 15$). Other micromechanical parameters are adopted from Li et al. (2022).

Journal Pre-proof

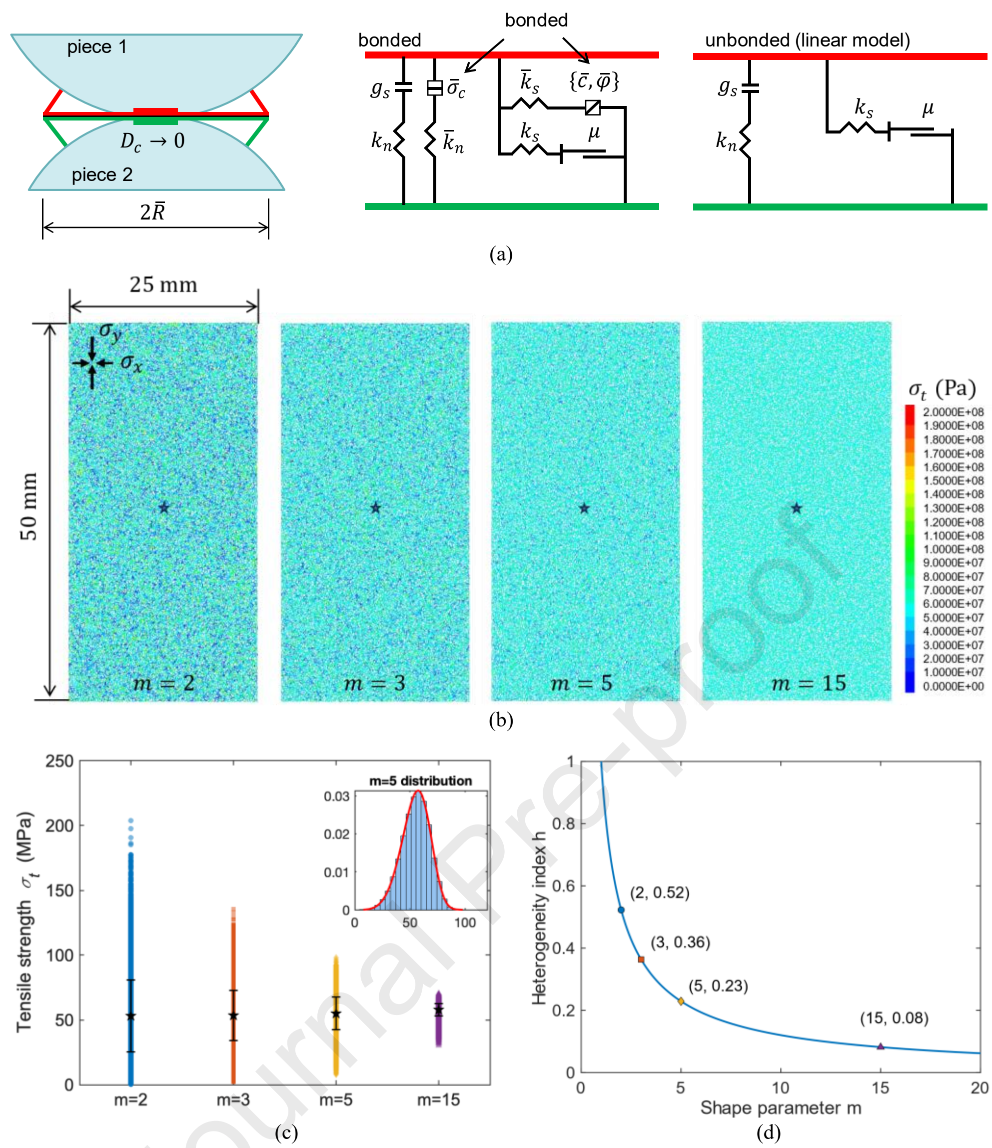

Fig. 1. (a) Rheological components of the linear parallel bond model (after Itasca Consulting Group Inc. (2014)), (b) Spatial distribution of contact strength within the specimen for different Weibull shape parameters m, (c) Statistical distribution of contact strength, and (d) Relationship between Weibull shape parameter m and material heterogeneity index h. The star symbol in (b) marks the fluid injection point at the geometric center of the model.

2.2 Coupled hydromechanical scheme

2.2.1 Coupled hydromechanical scheme for power-law rheology

The hydromechanical interaction is modeled using a discrete element-pore network coupling strategy, wherein the interstitial voids bounded by particle assemblies form discrete pore domains, representing the geometric dual of the contact framework as shown in Fig. 2 (Zhang et al., 2013; Wang et al., 2022). Hydraulic connections between adjacent pores are conceptualized as throats located at interparticle contacts. Each throat is approximated by a parallel-plate conduit, for which laminar flow behavior is described by a generalized Poiseuille-type relation.

For non-Newtonian fracturing fluids following a power-law rheology, the shear stress-shear rate relationship takes the form:

$$\tau_{\mathrm{f}} = K_{\mathrm{c}}\dot{\gamma}_{\mathrm{f}}{}^{n} \qquad (4)$$

where τ_{f} is the fluid shear stress; $\dot{\gamma}_{\mathrm{f}}$ is the shear rate; and K_{c} and n are the consistency and flow-behavior indices. The discharge rate q through a conduit of aperture w and length L_{p} satisfies (Li et al., 2024b):

$$q|q|^{n-1} = \frac{w^{2n+1}}{M'}\frac{p_1 - p_2}{L_{\mathrm{p}}} \qquad (5)$$

where p_1 and p_2 are the pressures in the connected domains; and M' is the modified consistency parameter expressed as follows, and setting $n = 1$ yields

Journal Pre-proof

the cubic-law form for Newtonian flow.

$$M' = \frac{2^{n+1}(2n+1)^n}{n^n} K_c \tag{6}$$

The aperture w varies dynamically with the mechanical contact state. Under compression, a nonlinear force-aperture relationship is prescribed, adopting the hyperbolic form widely used in DEM hydromechanics (Al-Busaidi et al., 2005):

$$w = \frac{w_0 F_0}{F + F_0} \tag{7}$$

where w_0 is the initial aperture, and F_0 is the normal force corresponding to $w = 0.5w_0$. When the contact is open or fractured, the aperture depends on the interparticle gap w_{m}:

$$w = \min(w_0 + \lambda w_{\mathrm{m}}, w_{\max}) \tag{8}$$

with $\lambda = 1.0$ and $w_{\max}$ denoting the computationally imposed upper limit.

Fluid pressure changes ΔP within a pore domain incorporate both net flux and volumetric deformation (Al-Busaidi et al., 2005):

$$\Delta P = \frac{K_{\mathrm{f}}}{V}\left(\sum q\,\Delta t - \Delta V\right) \tag{9}$$

where K_{f} is the fluid bulk modulus, V is the domain volume, ΔV is the change in domain volume over the time step, and $\sum q\Delta t$ represents the net fluid inflow.

The critical explicit timestep Δt is governed by the hydraulic conductivity of the fracture network. The stability criterion scales according to the following relationship:

$$\Delta t \propto \frac{V}{K_{\mathrm{f}}}\left(\frac{M' {L_{\mathrm{p}}}^n}{w^{2n+1}|\nabla P|^{1-n}}\right)^{1/n} \tag{10}$$

where $|\nabla P| = |p_1 - p_2|/L_{\mathrm{p}}$ is the magnitude of the local pressure gradient. For the Newtonian fluid ($n = 1$), Eq. (10) reduces to the classical scaling $\Delta t \propto \frac{V}{K_{\mathrm{f}}}\frac{M' L_{\mathrm{p}}}{w^3}$ (Peirce and Siebrits, 2005; Li et al., 2025b). This relationship indicates that for low-viscosity fluids (small M') or large fracture apertures (large w), the critical timestep becomes prohibitively small. This imposes a significant computational challenge for simulating fracture propagation, particularly in the toughness-dominated regime where low-viscosity fluids are often involved.

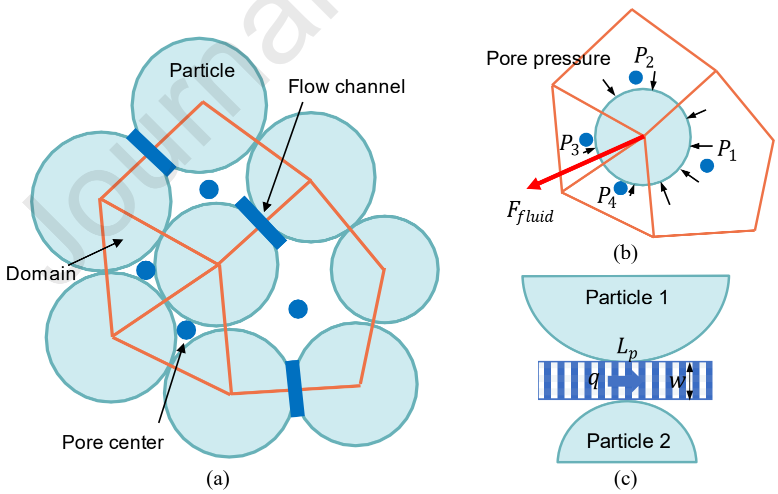

Fig. 2. Pore network model constructed from DEM: (a) Enclosed domains formed by neighboring particles, (b) Drag force on a particle derived from the pressures of adjacent domains, and (c) Fluid flow in an activated channel following bond breakage.

2.2.2 Improved algorithm for toughness-dominated regime

In scenarios where rock toughness dominates over viscous dissipation, either due to a high fracture toughness or a low effective viscosity of the injected fluid, the pressure distribution within the fracture tends to be nearly uniform. Under such conditions, fracture advance is governed primarily by the energy required to create new crack surfaces, and its behavior closely follows that of a Griffith-type crack. Conventional hydromechanical coupling formulations become computationally restrictive in this regime because numerical stability demands extremely small fluid time increments to suppress non-physical pressure oscillations (Eq. (10)).

To improve numerical performance, a modified coupling strategy is adopted for toughness-dominated propagation (Li et al., 2020, 2022). This approach assumes a spatially uniform fluid pressure and treats the fracture-fluid system as hydraulically closed due to the negligible permeability of the host rock.

Journal Pre-proof

Rather than resolving local gradients, the fluid pressure is updated globally from the mismatch between the cumulative injected fluid volume V_{f}, and the current open fracture volume V_{c}:

$$\Delta P = \kappa\,(V_{\mathrm{f}} - V_{\mathrm{c}})/V_{\mathrm{t}} \tag{11}$$

where $V_{\mathrm{t}} = \sum L_{\mathrm{P}} w$ is the total fracture volume, and $V_{\mathrm{c}} = V_{\mathrm{t}} - \sum L_{\mathrm{P}} w_0$ represents the net volume increment beyond the initial aperture w_0. The parameter κ is a numerical relaxation coefficient representing the effective stiffness of the fracture system, used to regulate the iterative pressure update to strictly enforce volume conservation.

The fluid time step (Δt) is dynamically determined by balancing volumetric growth of the fracture with the injection rate (Q_0):

$$\Delta t = \min\left(\frac{V_{\mathrm{c}}}{Q_0}, \Delta t_{\max}\right) \tag{12}$$

where $\Delta t_{\max}$ is a prescribed upper limit to ensure numerical accuracy. Compared to conventional explicit schemes, this approach allows for fluid time steps that are more than two orders of magnitude larger, thereby substantially reducing the total computational cost. It should be noted, however, that this method is strictly applicable within the toughness-dominated regime or in scenarios where viscous effects are negligible.

The fully hydromechanical coupling framework is illustrated in Fig. 3. Initially, all hydraulic throats are set to an inactive state, precluding any fluid transmission. When a bonded contact fails, microcracks emerge, activating the associated throats and enabling localized fluid exchange. This process dynamically couples mechanical fracture propagation with hydraulic connectivity evolution. At each coupling step, fluid pressures are updated, and the resulting equivalent body forces are imposed on the surrounding particles, ensuring consistent bidirectional feedback between fracture propagation, hydraulic connectivity, and fluid redistribution.

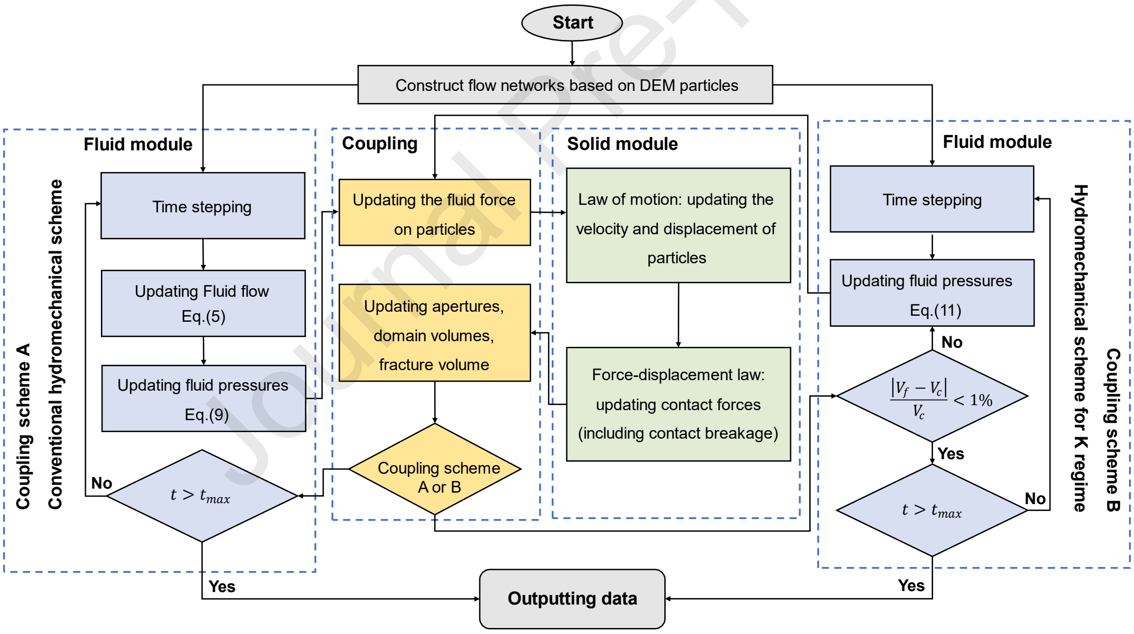

Fig. 3. The fully coupled hydromechanical framework.

3. Model validation within the parametric space

3.1 Dimensionless parametric space

Hydraulic fracture propagation is affected by fluid viscosity, fracture toughness, and fluid leak-off (Detournay, 2016), which together determine the balance between energy dissipation and fluid storage. Depending on the geological and operational conditions, different mechanisms may dominate. To systematically identify the dominant regime and simplify analysis, the concept of a parametric space has been introduced.

A common strategy for constructing such a parametric space is to assume a simplified fracture geometry, which reduces the governing equations from integral or differential form to closed-form algebraic expressions (Dontsov, 2017, 2019). In our earlier work (Li et al., 2024b), a Griffith-type toughness-

Journal Pre-proof

dominated fracture geometry was adopted, and regime boundaries were derived by comparing aperture predictions from near-tip asymptotics with limiting solutions for the case of power-law fluid rheology and plane strain fracture geometry. This yields the parametric space shown in

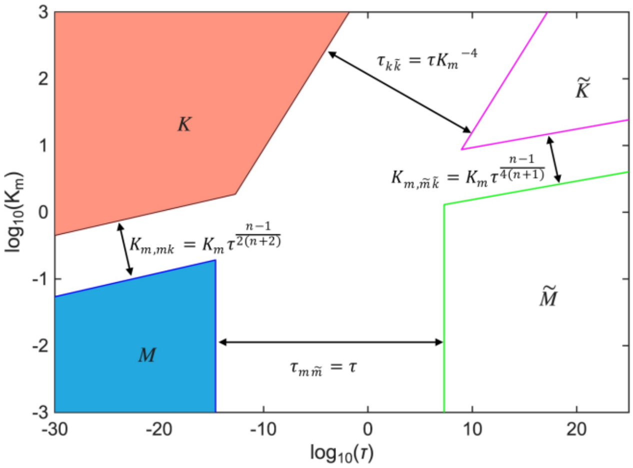

Fig. 4, where fracture growth behavior is categorized into viscosity-dominated (M), toughness-dominated (K), or leak-off- dominated ($\widetilde{M}$ and $\widetilde{K}$) regimes, with transitional zones regions indicating mixed control. The parametric space is defined by two dimensionless variables:

$$\tau = \left[\frac{E' C'^{2(n+2)}}{M' Q_0^{n+2}}\right]^{1/n} t \tag{13}$$

$$K_{\mathrm{m}} = \left[\frac{K'^{4n}}{C'^{4(n-1)} E'^{4n-1} Q_0^{2-n} M'}\right]^{1/(4n)} \tag{14}$$

where the dimensionless time τ characterizes fluid leak-off and the dimensionless toughness K_{m} quantifies the competition between viscous and fracture energy dissipation. Here Q_0 is the fluid injection rate; t is the injection time; and $E' = E/(1-\upsilon^2)$, $K' = 4(2/\pi)^{1/2} K_{\mathrm{IC}}$ and $C' = 2C_{\mathrm{L}}$ are the material parameters, with E, υ, K_{IC} and C_{L} denoting Young's modulus, Poisson's ratio, mode-I toughness of the rock, and Carter's leak-off parameter, respectively.

When fluid leak-off is neglected, the competition between fluid viscosity and fracture toughness in driving fracture propagation can be characterized by a dimensionless parameter $K_{\mathrm{m,mk}}$:

$$K_{\mathrm{m,mk}} = K_{\mathrm{m}} \tau^{\frac{n-1}{2(n+2)}} \tag{15}$$

For Newtonian fluids ($n = 1.0$), this expression simplifies to $K_{\mathrm{m,mk}} = K_{\mathrm{m}}$ and remains constant over time, whereas for power-law fluids ($n \neq 1.0$), $K_{\mathrm{m,mk}}$ evolves with time. In the case of shear-thinning fluids ($n < 1.0$), fracture propagation typically transitions from an early-time toughness-dominated regime to a late-time viscosity-dominated regime (Garagash, 2006).

The numerical boundaries distinguishing viscosity- (M) and toughness-dominated (K) regimes vary slightly among studies: Hu and Garagash (2010) proposed $\mathrm{K}_{\mathrm{m,mk}} \leq 1.2$ for viscosity dominance and $K_{\mathrm{m,mk}} \geq 3.8$ for toughness dominance; Dontsov (2017) suggested $K_{\mathrm{m,mk}} \leq 0.70$ and $K_{\mathrm{m,mk}} \geq 4.80$; Li et al. (2024b) determined boundaries of $K_{\mathrm{m,mk}} < 0.72$ and $K_{\mathrm{m,mk}} > 4.57$. The differences originate predominantly from using various metrics to define the boundaries. Since the parametric space is presented in logarithmic coordinates, such small differences are acceptable in practice. For non-Newtonian fluids, the regime boundaries depend on n: For behavior index $n = 0.8$, the fracture propagates in the viscosity-dominated regime if $K_{\mathrm{m,mk}} < 0.64$ and in the toughness-dominated regime if $K_{\mathrm{m,mk}} > 5.08$. For behavior index $n = 0.6$, the fracture propagates in the viscosity-dominated regime for $K_{\mathrm{m,mk}} < 0.56$ and in the toughness-dominated regime for $K_{\mathrm{m,mk}} > 6.11$ (Li et al., 2024b). A smaller n increases the separation between these boundaries, expanding the toughness-dominated regime while narrowing the viscosity-dominated regime, as illustrated in Fig. 3.

Journal Pre-proof

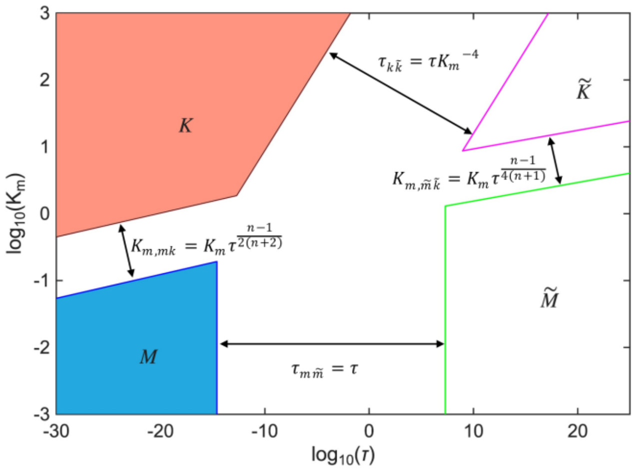

Fig. 4. Phase diagram of fracture propagation regimes for a plane strain fracture driven by a power-law fluid with $n = 0.8$. M represents the viscosity-dominated regime, K represents the toughness-dominated regime, $\widetilde{M}$ represents the leak-off viscosity-dominated regime, and $\widetilde{K}$ represents the leak-off toughness-dominated regime.

3.2. Numerical model validation

To validate the numerical model, simulations were first conducted for Newtonian fluids ($n = 1$) using regularly arranged particles with uniform properties. The particle radius was fixed at 0.133 mm, with other input parameters shown in Table 1 (Li et al., 2022). Three fracturing fluids with distinct viscosities (500 cp, 100 cp, and 0.06 cp) were simulated to cover different propagation regimes along the MK edge in the parametric space (Fig. 5a). Given a mode-I fracture toughness of 1.70 MPa m$^{0.5}$, the corresponding dimensionless toughness $K_{\mathrm{m,mk}}$ were calculated as 1.44, 2.15, and 13.77, respectively. Although the first two cases (500 cp and 100 cp) technically fall within the transition regime, the 500 cp case ($K_{\mathrm{m,mk}} = 1.44$) is situated much closer to the viscosity-dominated limit (M-vertex in Fig. 5a), exhibiting significant viscous dissipation. In contrast, the 0.06 cp case lies clearly inside the toughness-dominated regime. Accordingly, conventional coupling scheme (Section 2.1) was employed for the first two cases, while the improved algorithm (Section 2.2) was used for the toughness-dominated scenario.

The numerical results demonstrate good agreement with analytical KGD solutions across all three regimes (Fig. 5b). For the 500 cp case ($K_{\mathrm{m,mk}} = 1.44$), the simulated fracture length of 3.01×10^{-2} m shows only a 1.56% deviation from the KGD prediction of 3.12×10^{-2} m, while the fracture width of 1.46×10^{-5} m exhibits a 10.2% overestimation compared to the theoretical value of 1.32×10^{-5} m. Similar agreement was observed for the toughness-dominated case ($K_{\mathrm{m,mk}} = 13.77$), where the model precisely matched the theoretical fracture length of 3.41×10^{-2} m, with a 6.10% overestimation in fracture width. The observed discrepancies in fracture width primarily stem from model formulation differences. The KGD solution assumes point-source injection, whereas our numerical model incorporates finite-length injection zones (two preset microcracks). Overall, the good agreement across viscosity- and toughness-dominated regimes confirms the ability of our coupled DEM-fluid model in accurately capturing diverse hydraulic fracturing behaviors.

Table 1. Input parameters for the numerical model.

Variable		Symbol (unit)	Value
Micro parameter	Particle radius	R (mm)	0.1-0.166
	Particle-particle contact modulus	E^* (GPa)	29
	Contact normal-to-shear stiffness ratio	k^*	2.0
	Particle friction coefficient	μ_{f}	0.6
	Particle density	ρ_{s} (kg/m^3)	2500
	Bond modulus	$\bar{E}^*$ (GPa)	29
	Bond normal-to-shear stiffness ratio	$\bar{k}^*$	2.0
	Bond tensile strength	σ_{t} (MPa)	60

Journal Pre-proof

	Bond cohesion	σ_c (MPa)	90
	Bond friction angle	$\bar{\varphi}$ (°)	30
	Shape parameter	m	2, 3, 5, 15
		h	0.52, 0.36, 0.23, 0.08
Hydraulic parameter	Assumed residual aperture	w_0 (m)	1×10^{-8}
	The bulk modulus of fluid	K_f (GPa)	2.2
	Proportionality coefficient	κ (MPa)	0.2
	Injection rate	Q_0 (m^2/s)	2×10^{-7}
	Injection fluid viscosity	μ (cp)	500, 100, 0.06
	Plane strain modulus	E' (GPa)	56
	Mode I fracture toughness	K_{IC} (MPa $m^{0.5}$)	1.70
	Dimensionless toughness	$K_{m,mk}$	1.44, 2.15, 13.77

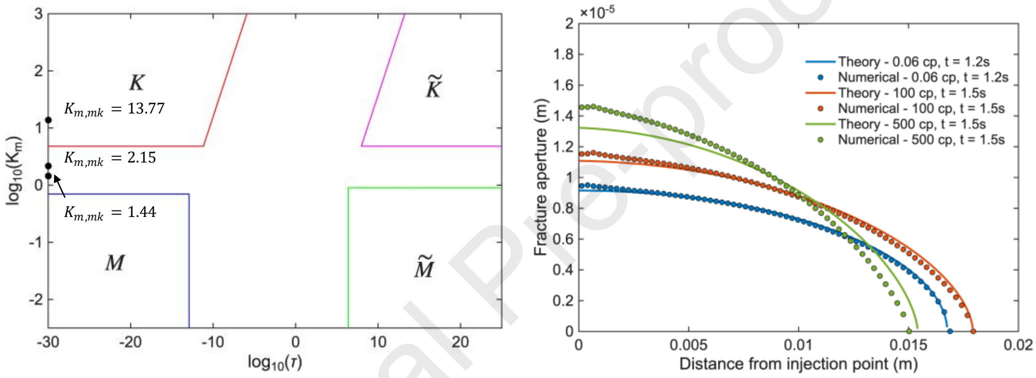

(a) (b)

Fig. 5. Simulation of Newtonian fluid injection in a homogeneous medium: (a) Locations of the three cases in the parametric space, and (b) Validation against the theoretical KGD solution (Dontsov, 2017).

4. Simulation results

Following model validation, a two-dimensional (2D) numerical model representing an intact rock specimen was generated with dimensions of 25 mm (width) × 50 mm (height). The model comprises a total of 19,410 particles, with radii following a uniform distribution between 0.1 mm and 0.166 mm. A fixed random seed was employed during generation to ensure reproducibility. To simulate in situ conditions, the specimen is subjected to confining stresses of $\sigma_x = 10$ MPa (horizontal) and $\sigma_y = 20$ MPa (vertical), resulting in a differential stress ratio of 2:1. Fluid injection is initiated at the geometric center of the model. Four distinct models with varying homogeneity indices ($m = 2, h = 0.52$; $m = 3, h = 0.36$; $m = 5, h = 0.23$; $m = 15, h = 0.08$) were constructed to represent different degrees of rock heterogeneity, as illustrated in Fig. 1. Additional simulation parameters are detailed in Table 1.

4.1 Influence of heterogeneity

In field-scale hydraulic fracturing operations, fractures generally propagate under conditions approaching the viscosity-dominated regime (Lecampion and Desroches, 2015). This results from the relatively high viscosity of commonly used fracturing fluids (e.g. cross-linked gels or slickwater with high concentrations of additives) and prolonged injection durations, both of which enhance fluid-driven fracture growth over toughness-dominated mechanisms. To investigate the role of rock heterogeneity, we first conducted simulations under near-viscosity-dominated conditions ($K_{m,mk} = 1.44$).

Fig. 6 shows the fracture morphology, aperture distribution, and fluid pressure profiles at $t = 1.5$ s for specimens with varying heterogeneity index h. These results reveal a pronounced transition from complex, diffuse fractures to simpler, planar fractures as the material becomes more homogeneous. In highly heterogeneous specimens ($h = 0.52$), fluid injection produces a fracture network consisting of a dominant main fracture and numerous secondary branches. The injected fluid primarily flows through the main fracture, which exhibits significant aperture dilation, while most branch fractures experience minimal opening and contribute little to fluid transport. This behavior arises from the abundance of weakly bonded contacts, as shown in Fig. 1c, analogous to weak natural interfaces and pre-existing flaws in real rocks. Ahead of the main fracture tip, a diffuse process zone develops where stress perturbations induce both tensile and shear failures of these weak contacts. Some of these microcracks coalesce with the main fracture, becoming hydraulically active and enhancing its growth. However, many remain isolated with no fluid penetration (i.e. pore pressure = 0), represented by the short black lines in Fig. 6. These are hereafter referred to as "dry microcracks", defined as mechanically induced bond breakages or microdefects that have not yet been invaded by the fracturing fluid. Localized microcracking in the process zone absorbs strain energy and produces crack-tip shielding, reducing the driving force for main-fracture extension. When the tip encounters a strong interface with limited microcrack connectivity, temporary arrest may occur until continued injection elevates the local pressure and reactivates propagation. Notably, the density of dry microcracks increases with distance from the injection point, consistent with experimental observations that often report enhanced fracture complexity and branching farther from the wellbore (Chen et al., 2020).

As the heterogeneity index h decreases, the distribution of interfacial strength becomes more uniform (Fig. 1b and c). This homogeneity suppresses the generation of stress-induced isolated microcracks and promotes more stable and predictable propagation. The resulting geometry approaches a discrete, bi-wing fracture. The reduction in geometric complexity is accompanied by a lower peak fluid pressure, since less energy is dissipated in activating branched fractures or off-plane weaknesses (Fig. 6). Correspondingly, the maximum aperture is also reduced due to more uniform fracture front advancement and the absence of strong barriers that trap fluid and induce local aperture enlargement.

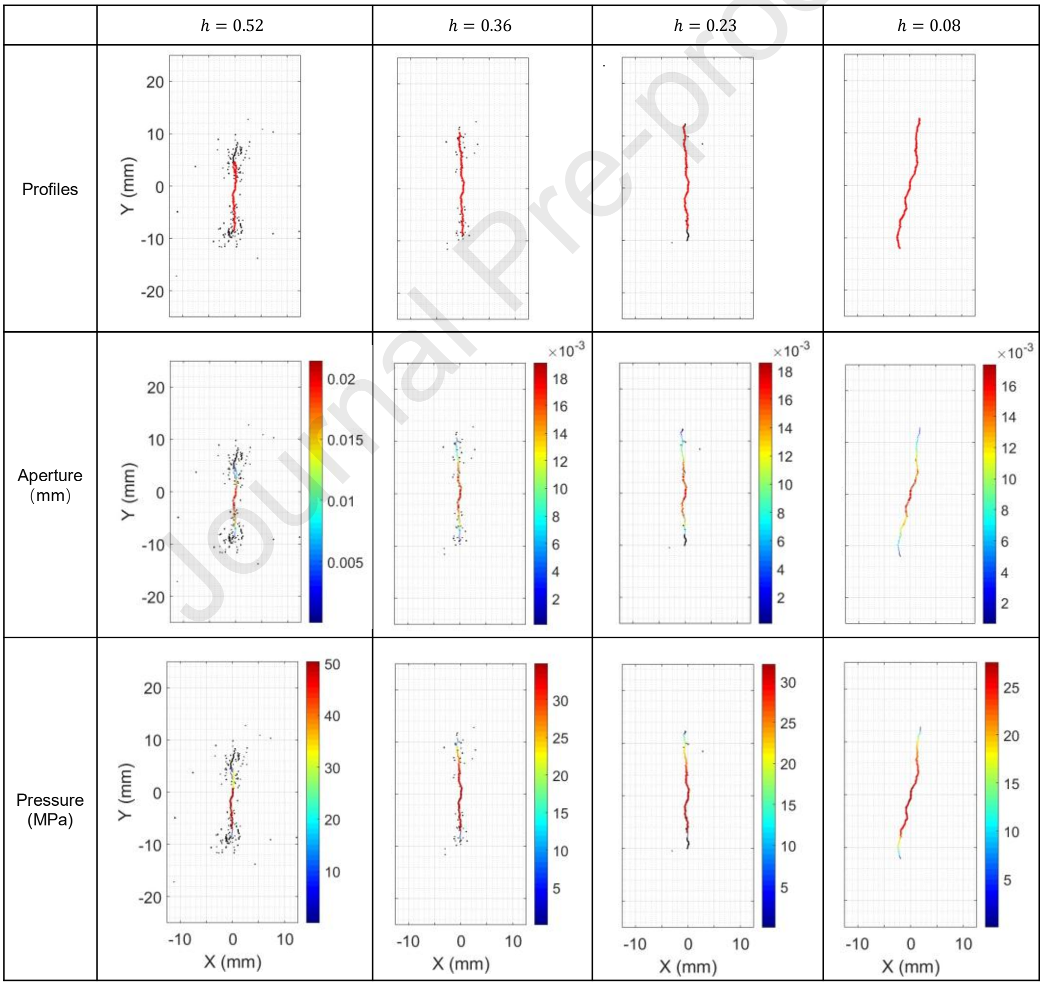

Fig. 6. Fracture morphology, aperture distribution, and fluid pressure fields at $t = 1.5$ s for high-viscosity (500 cp) fluid injection across different heterogeneity levels.

4.2 Propagation regimes with Newtonian fluids

To examine the influence of propagation regimes, 12 numerical simulations were conducted with Newtonian fluids spanning viscosity- to toughness-dominated conditions. Fig. 7 demonstrates a morphological transition at $t = 1.5$ s. Fractures driven by high-viscosity fluids propagate nearly symmetrically about the injection point, while those driven by low-viscosity fluids exhibit pronounced asymmetry. Even in nominally homogeneous specimens ($h = 0.08$),

Journal Pre-proof

directional propagation persists under toughness-dominated conditions, reflecting the influence of stochastic variations in particle packing. This emphasizes the critical role of microstructural randomness in determining fracture path selection. This behavioral divergence arises from the distinct pressure distributions characteristic of each regime. In toughness-dominated regimes, the nearly uniform fluid pressure profile renders fracture growth highly sensitive to local heterogeneities ahead of the fracture tip, consistent with experimental observations (Bunger and Detournay, 2008) and numerical studies (Huang et al., 2019; Tanné et al., 2022).

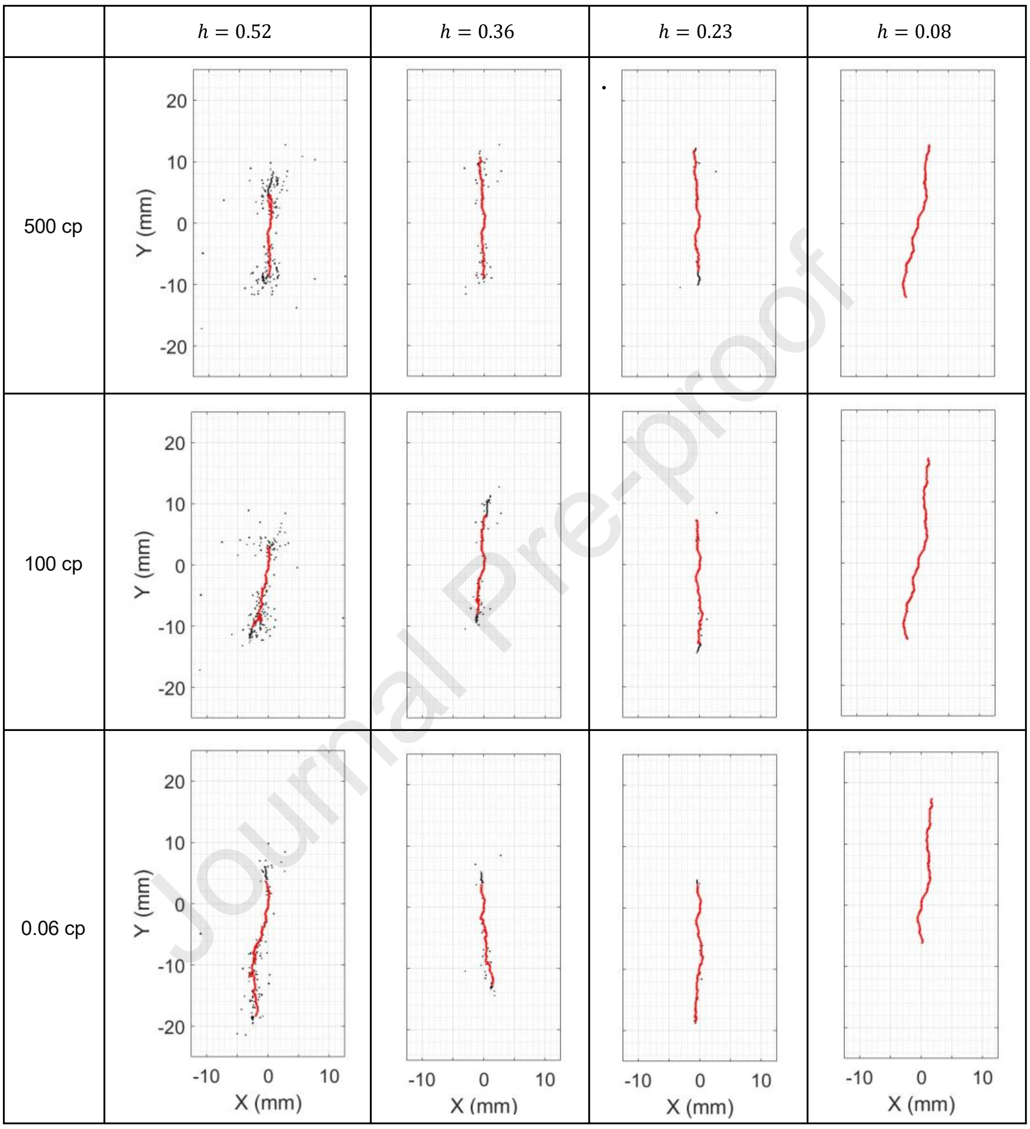

Fig. 7. Fracture morphology at $t = 1.5$ s for Newtonian fluid injection under different heterogeneity conditions and different fluid viscosities. Short red lines indicate fluid-invaded microcracks, while short black lines denote dry microcracks without fluid penetration.

Fig. 8 provides a close-up view along the negative y-axis for the highly heterogeneous specimen ($h = 0.52$), showing that in near-viscosity-dominated regime, dry microcracks are abundant, and their density generally increases with distance from the injection point. As the system approaches the toughness-dominated regime, dry microcracks become more localized around the main fracture, and their spatial variation with distance is less pronounced. Some isolated microcracks remain unpressurized and disconnected from the main fracture, highlighting heterogeneous local responses. Low-viscosity fluids also promote local particle detachment, producing fragment-like features analogous to laboratory observations (Zhuang et al., 2020).

Fig. 9 further quantifies the fraction of dry microcracks across different heterogeneity levels and fluid viscosities. In highly heterogeneous specimens ($h = 0.52$), weak bonds fail readily under stress perturbations, generating numerous microcracks, some exceeding the number in the main fracture (e.g. 100 cp and 500 cp cases). Some of these later coalesce into complex networks, consistent with previous numerical findings (Wang et al., 2025a). As homogeneity increases, the fraction of dry microcracks decreases, reflecting a more uniform and stable fracture process zone. Fluid viscosity further modulates these patterns: viscosity-dominated fractures exhibit larger pressure gradients and wider apertures, resulting in higher densities of dry microcracks, whereas toughness-dominated fractures show smaller pressure variations and more confined distributions. These results underscore the coupled influence of fracture propagation regimes and material heterogeneity on both the spatial distribution and overall abundance of dry microcracks, influencing fracture complexity and pressure evolution.

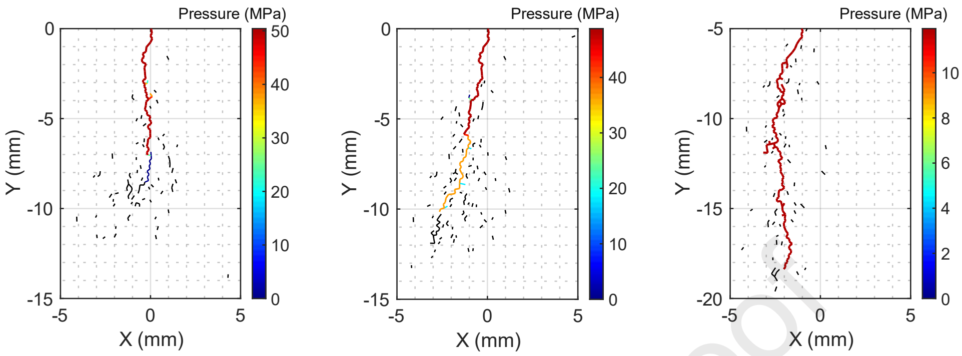

(a) (b) (c)

Fig. 8. Fluid pressure distributions at $t = 1.5$ s resulting from Newtonian fluid injection into the highly heterogeneous specimen ($h = 0.52$) for different viscosities: (a) 500 cp, (b) 100 cp, and (c) 0.06 cp.

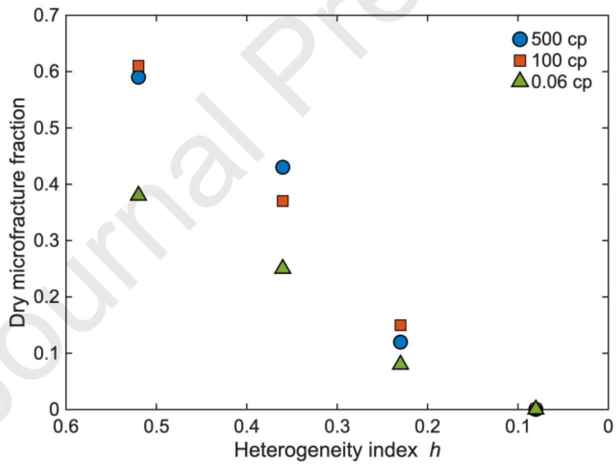

Fig. 9. The fraction of dry microcracks under different heterogeneity conditions.

4.3 Propagation regimes with shear-thinning fluids

For shear-thinning power-law fluids, the Poiseuille's law (Eq. (5)) indicates that the flow rate becomes increasingly sensitive to the pressure gradient as the behavior index n decreases. To ensure numerical stability in the explicit fluid-solid coupling scheme, smaller fluid time steps are required, which increases computational cost. Therefore, a relatively high consistency index ($K_c = 1.0$ Pa s^n, $n = 0.8$) is adopted for Case A, and two cases are examined as listed in Table 2. Case A lies close to the viscosity-dominated regime in the parametric space, whereas Case B approaches the toughness-dominated regime (Fig. 10).

Table 2. Simulation parameters for the power-law fluid cases.

Variable	Symbol (unit)	Case A	Case B
Behavior index	n	0.8	0.8
Consistency index	K_c (Pa s^n)	1.0	0.1
Mode I fracture toughness	K_{IC} (MPa m$^{0.5}$)	1.70	1.70

Journal Pre-proof

Injection rate	Q_0 (m²/s)	2 × 10⁻⁶	2 × 10⁻⁷
Flow time	t (s)	0.07	0.7
Dimensionless toughness	$K_{\mathrm{m,mk}}$	1.16	3.53

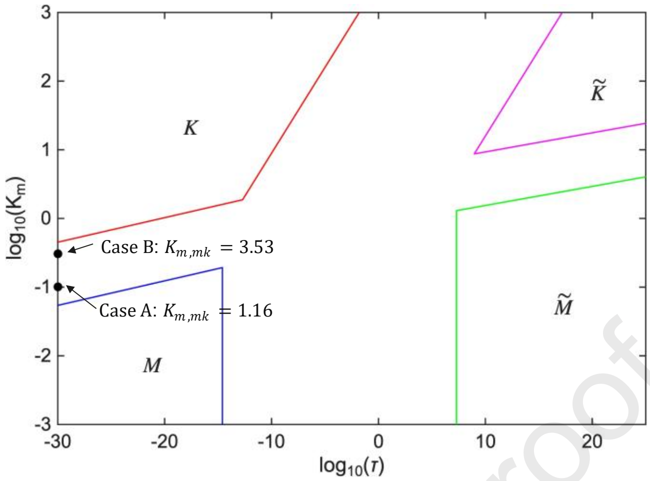

Fig. 10. Locations of Case A and Case B within the parametric space for the case of shear-thinning fluid with $n = 0.8$.

The fracture morphologies of the two cases are shown in Fig. 11. The fracture morphology in the toughness-dominated regime is identical to that in Fig. 7, as fracture toughness overwhelms viscous dissipation, rendering propagation largely insensitive to fluid rheology. In contrast, near the viscosity-dominated regime, fractures propagate more symmetrically and develop additional branches, especially in highly heterogeneous specimens ($h = 0.52$). However, compared with Newtonian fluids, power-law fluids produce fewer branches. This behavior can be explained by the time-evolving propagation regime of power-law fluids, which transitions from early-time toughness-dominated to late-time viscosity-dominated growth, as quantified in Eq. (15). Furthermore, steeper tip pressure gradients near the fracture tip and shear-thinning-induced reduction in apparent viscosity together suppress the morphological differences between the two endmember regimes. In the transition regime, fracture propagation exhibits intermediate behavior, with reduced branching and asymmetric growth. While heterogeneity exerts similar influence for both Newtonian and power-law fluids, the regime boundaries in the parametric space remain highly sensitive to the behavior index n.

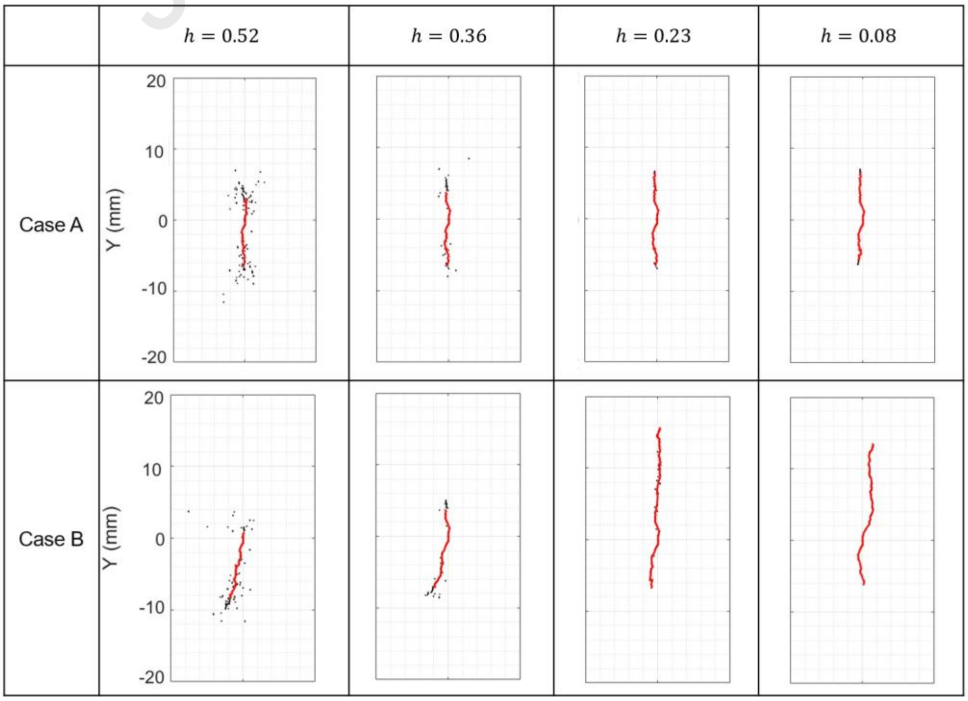

Fig. 11. Fracture morphology for shear-thinning power-law fluid injection under different heterogeneity conditions ($n = 0.8$). Short red lines indicate fluid-invaded microcracks, while short black lines denote dry microcracks without fluid penetration.

5. Discussion

5.1 Apparent fracture toughness

Increasing heterogeneity promotes the generation of stress-induced isolated microcracks, resulting in shorter main fractures and a more uniform internal pressure distribution, as shown in Fig. 6. This behavior reflects an increase in the macroscopic resistance of the rock to fracture propagation with the heterogeneity index h, corresponding to an enhancement in the apparent fracture toughness. Previous DEM studies have shown that even geometric randomness alone can increase the apparent toughness. For instance, Huang et al. (2019) reported that random particle packing produced approximately 30% higher apparent toughness than regular lattices owing to the stochastic redistribution of load-bearing paths. The present simulations are consistent with this trend and further reveal that mesoscale heterogeneity in bond properties, represented by a Weibull distribution, introduces an additional toughening effect beyond that caused by particle randomness.

The enhancement of apparent fracture toughness arises from additional energy-dissipation channels activated by heterogeneity. Microcracks surrounding the dominant fracture tip act as localized energy sinks, absorbing strain energy through crack deflection, tortuosity, and branching before the main fracture extends. These mechanisms resemble the "toughening-by-tortuosity" and "microcrack trapping" effects reported in phase-field analyses of heterogeneous materials (Hossain et al., 2014; Liu and Shen, 2025). Recently, Liu and Shen (2025) demonstrated that even for the quasi-most-fragile microstructural configurations, those representing the weakest possible arrangements of heterogeneity that facilitate fracture propagation, the macroscopic apparent fracture toughness remains elevated owing to local dissipative processes.

To further quantify this effect, hydraulic fracturing tests using regular lattices were conducted, as shown in Fig. 12. Here, the numerical fracture aperture w, calculated dynamically via Eqs. (7) and (8), serves as the primary input for determining the fracture resistance. The apparent fracture toughness ($K_{\mathrm{IC,app}}$) was derived through an inverse analysis, where the numerical fracture aperture evolution was fitted to the KGD analytical solution. The results indicate that the apparent toughness increases from 1.7 MPa $m^{0.5}$ for the homogeneous case ($h = 0$; Section 3) to varying degrees depending on fluid viscosity when $h = 0.36$: about 4.5 MPa $m^{0.5}$ for 500 cp, 3.1 MPa $m^{0.5}$ for 100 cp, and 3.0 MPa $m^{0.5}$ for 0.06 cp. The viscosity dependence arises because higher-viscosity fluids enlarge the fracture process zone, thereby amplifying the influence of distributed microcrack dissipation, which will be discussed further in Section 5.2.

Although the particles are arranged regularly, local variations in bond properties still create weak links both parallel and perpendicular to the main fracture, facilitating the formation of isolated microcracks and localized damage. The apparent toughness reported here represents an effective, system-level value inferred from hydraulic fracture propagation rather than a fundamental material constant. The insightful work of Wei et al. (2021) provides an important experimental reference: they demonstrated that the measured fracture toughness can vary substantially with loading configuration due to the coupled influence of T-stress and the fracture process zone. This finding underscores that even nominally homogeneous specimens exhibit dependence of apparent toughness on local stress states and inelastic energy dissipation (Wei et al., 2023). The present findings indicate that mesoscale heterogeneity enhances the local energy barrier to fracture extension through diffuse damage and localized energy absorption. This toughening effect aligns with field-scale observations where inversions of kilometer-scale dikes yield effective toughness values one to three orders of magnitude higher than laboratory measurements (Rivalta et al., 2015). Therefore, the system-level apparent toughness emerges as a physically meaningful measure of macroscopic fracture resistance, since it intrinsically captures the influence of microstructural heterogeneity, a factor demonstrated to be essential for reproducing realistic fracture propagation (Dontsov and Suarez-Rivera, 2021).

Journal Pre-proof

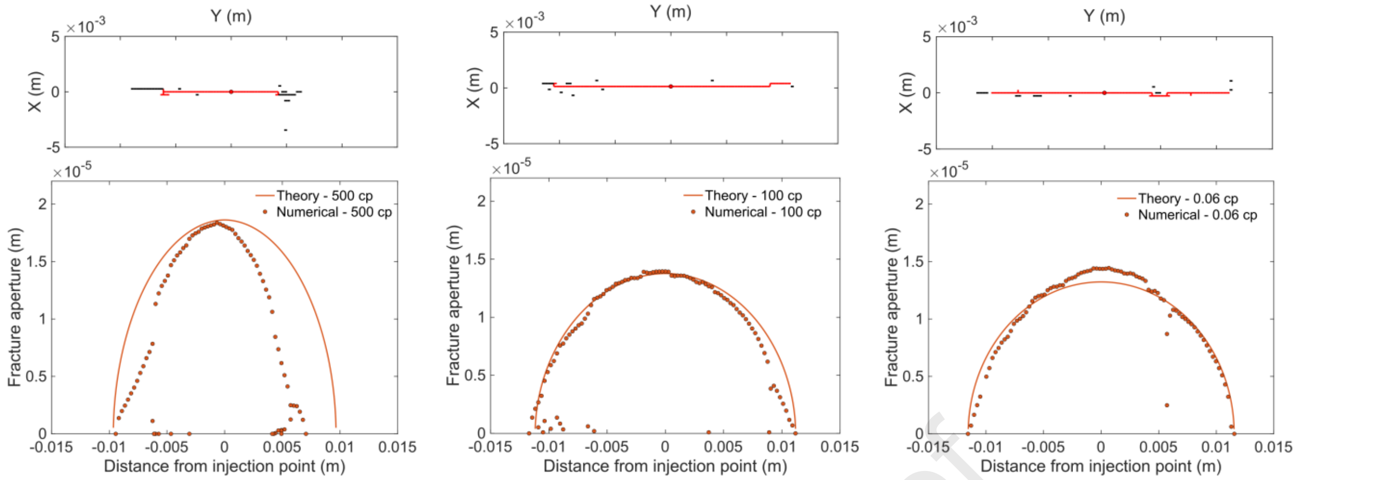

(a) (b) (c)

Fig. 12. Fracture morphology and corresponding KGD comparisons (Dontsov, 2017) for the heterogeneous regular-lattice case ($h = 0.36$) at $t = 1.2$ s under different fluid viscosities: (a) 500 cp, $K_{\mathrm{IC,app}} = 4.5$ MPa m$^{0.5}$, $K_{\mathrm{m,mk}} = 3.82$; (b) 100 cp, $K_{\mathrm{IC,app}} = 3.1$ MPa m$^{0.5}$, $K_{\mathrm{m,mk}} = 3.94$; and (c) 0.06 cp, $K_{\mathrm{IC,app}} = 3.0$ MPa m$^{0.5}$, $K_{\mathrm{m,mk}} = 24.34$. Short red lines indicate fluid-invaded microcracks, while short black lines denote dry microcracks without fluid penetration.

5.2 Fracture complexity

While Section 5.1 focused on how heterogeneity enhances the apparent fracture toughness through additional energy-dissipation mechanisms, this section examines how the same mesoscale effects influence the geometric complexity of hydraulic fractures under Newtonian and power-law fluids. It is important to note that all simulated cases are assumed to remain within the same dominant propagation regime.

Typically, hydraulic fracture modeling is grounded in LEFM (Rice, 1968), where the crack-tip solutions yield a kidney-shaped stress field ($\sigma \propto r^{-1/2}$) and an opening profile as shown in Fig. 13 ($w \propto r^{1/2}$). Within this perturbation zone, weak interfaces may fail, producing tensile microcracks (Zhuang and Zang, 2021). Increasing heterogeneity enlarges this activated zone, leading to more distributed damage. However, the extent and nature of these perturbations are regime-dependent. According to Dontsov and Kresse (2018), the tip asymptotes for a power-law fluid differ between toughness and viscous regimes:

$$\overline{w}_{\mathrm{k}}(x) = \frac{K'}{E'} x^{1/2} \qquad (16)$$

$$\overline{w}_{\mathrm{m}}(x) = \left[\frac{2(2+n)^2}{n} \tan\left(\frac{\pi n}{2+n}\right)\right]^{\frac{1}{2+n}} \left(\frac{\dot{x}^n M'}{E'}\right)^{\frac{1}{2+n}} x^{\frac{2}{2+n}} \qquad (17)$$

where $\overline{w}_{\mathrm{k}}$ and $\overline{w}_{\mathrm{m}}$ are the toughness and viscous asymptote, respectively; x is the distance from the fracture tip; and $\dot{x}$ is the fracture tip velocity. In toughness-dominated propagation, typically associated with low-viscosity fluids, stress perturbations remain localized, leading to relatively few secondary cracks. However, the main fracture path becomes highly sensitive to local heterogeneity, often producing asymmetric or unstable propagation (Ishida et al., 2016). By contrast, viscosity-dominated propagation, often induced by high-viscosity fluids or injection rate, deviates from the classical LEFM asymptote since the extent of the $w \propto r^{1/2}$ zone is very limited (Hu and Garagash, 2010). The fracture opening scales as $w \propto r^{2/(2+n)}$, which reduces to $w \propto r^{2/3}$ for Newtonian fluids (Eq. (17)), while the stress singularity is

$$\sigma \propto r^{-\frac{n}{2+n}} \quad (n \leq 1) \qquad (18)$$

This distributes energy over a broader process zone, which suppresses large path deviations but activates dispersed dry cracks around the main fracture. Consequently, fracture complexity in viscosity-dominated regimes primarily arises from distributed microcracking, whereas in toughness-dominated regimes it stems from tip instability.

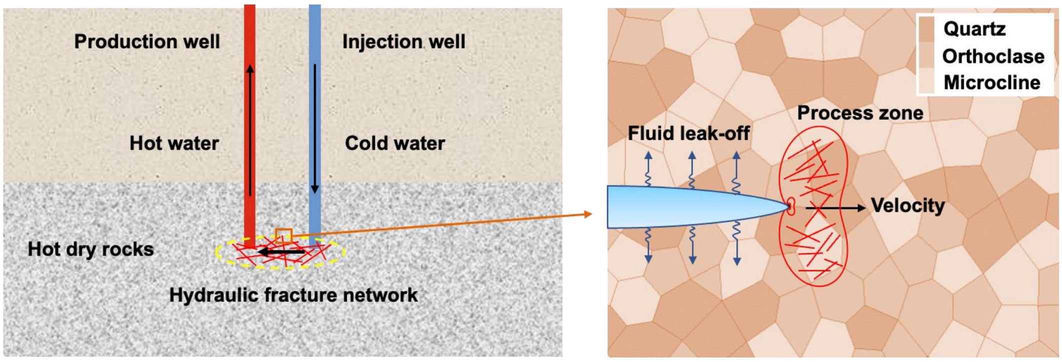

(a) (b)

Fig. 13. Schematic diagrams of EGS process: (a) Thermal circulation system, and (b) Hydraulic fracturing at grain scale with fracture-tip process zone (after Li et al., 2025a).

To quantify these geometric features, two complementary metrics were employed: tortuosity (T) and orthogonal roughness (R). Tortuosity (T), defined as the ratio of the total length of microcracks connected to the main fracture to the straight-line distance between its two tips (Chen et al., 2015), characterizes the degree of fracture path deviation and branching. Using principal component analysis, the first principal component is taken as the primary propagation direction, and orthogonal roughness (R) is defined as the root mean square of pointwise deviations perpendicular to this axis, normalized by the total fracture length. This measure reflects the degree of lateral irregularity or scattering of dry microcracks (Fig. 14). Results indicate that in highly heterogeneous media, viscosity-dominated fractures show high R but low T, reflecting broad microcrack activation without strong deflection of the main fracture, whereas toughness-dominated fractures exhibit higher T as the primary fracture is more readily diverted by heterogeneity. Due to the relatively high stress contrast applied in our simulations (10 MPa), as the material becomes more homogeneous, the differences in fracture morphology across propagation regimes diminish, resulting in nearly overlapping T and R values. Interestingly, cases located in the intermediate regime, such as the 100-cp fluid scenario, may simultaneously exhibit relatively high values of both T and R, indicating a combination of main-fracture deviation and lateral microcrack dispersion.

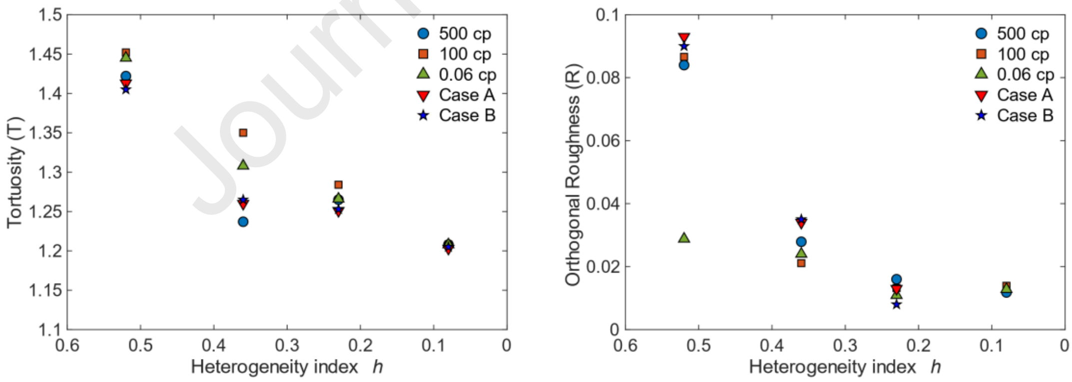

(a) (b)

Fig. 14. Tortuosity (a) and orthogonal roughness (b) of hydraulic fractures under varying heterogeneity for different fluids.

These results help refine the widely held assumption that low-viscosity fluids inherently produce more complex fracture networks. Instead, fracture complexity emerges from the coupled interplay of fluid rheology, stress anisotropy, heterogeneity, and propagation regime (Wu et al., 2022). For instance, significant complexity is most likely when toughness-dominated growth (often induced by low-viscosity fluids) interacts with pronounced material heterogeneity, consistent with numerical predictions (Chen et al., 2020). However, under high stress contrast conditions, the influence of heterogeneity is limited, and low-viscosity fluids primarily induce asymmetric rather than branched fractures. In contrast, high-viscosity fluids generate straighter dominant fractures while activating a wide process zone of distributed microcracks, which can enhance overall conductivity by creating secondary damage zones without large-scale branching.

This mechanistic framework is particularly relevant for engineered systems like EGS, where achieving optimal fracture network geometry is critical for efficient thermal energy extraction. (Fig. 13). The type of process zone generated at the fracture tip, whether diffuse or localized microcracking, directly dictates this geometry and thus the efficacy of the thermal circulation system. Consequently, operational parameters must be tailored to reservoir conditions: low-viscosity fluids may encourage complex networks in heterogeneous reservoirs though potentially compromising stability, whereas higher-viscosity fluids or increased injection rates can be used in more homogeneous settings to mobilize distributed microcracking and enhance conductivity. These considerations are particularly important for EGS operations, where fluid viscosities are typically low and fracture propagation is often toughness-dominated (Tanné et al., 2022).

Finally, certain limitations of the model warrant mention. First, fluid leak-off was neglected to strictly isolate the competition between viscosity and toughness storage mechanisms. Fluid infiltration, particularly with low-viscosity fluids, increases local pore pressure, thereby reducing effective stress and promoting interactions with weak sites (Zhuang and Zang, 2021). Neglecting this mechanism implies that our current results may represent a conservative estimate of fracture network complexity in permeable formations. Conversely, excessive fluid loss would shift the system toward leak-off-dominated regimes ($\widetilde{M}$ or $\widetilde{K}$ in Fig. 4), potentially reducing the global energy available for fracture extension. Second, the Weibull distribution used to characterize mechanical properties necessitates calibration against micromechanical data (Li et al., 2024a). Future work could integrate mineralogical variability and coupled poromechanical effects to more accurately capture microstructural heterogeneity. Third, these 2D simulations adopt the plane-strain assumption (KGD model), physically representing scenarios where fracture height is far greater than fracture length. While a 3D fluid front might vertically bypass local obstacles, potentially mitigating the "shielding" effect of heterogeneity seen in 2D, the fundamental mechanism by which heterogeneity governs the transition between dissipation regimes remains valid. Despite these simplifications, the current findings offer a valuable mesoscopic framework for elucidating how fluid properties and rock heterogeneity jointly control fracture network formation.

6. Conclusions

This study established a fully coupled DEM for hydraulic fracturing, incorporating a Weibull distribution of rock mechanical properties and accounting for both Newtonian and power-law fluid rheologies. The model was validated against classical KGD solutions and applied to investigate the mesoscale interaction between hydraulic fractures and heterogeneous rock structures under different propagation regimes. The main findings are summarized as follows:

(1) Increasing rock heterogeneity elevates the macroscopic resistance to fracture propagation by activating additional energy-dissipation mechanisms such as microcrack deflection, tortuosity, and branching. This effect manifests as higher apparent fracture toughness values and shorter but more distributed fracture networks.

(2) The influence of heterogeneity on fracture complexity depends on fracture propagation regimes. In viscosity-dominated regimes, a large process zone with relaxed stress singularity promotes distributed microcracking (high orthogonal roughness R), whereas in toughness-dominated regimes, uniform fluid pressure and localized stress perturbations cause asymmetric and unstable propagation paths (high tortuosity T).

(3) For power-law fluids, the spatial extent of the viscosity- and toughness-dominated regimes is governed by the flow behavior index (n). The shear-thinning nature of such fluids reduces the apparent viscosity near the fracture tip, and the time-evolving propagation regimes together diminish the morphological contrast between the two regimes compared with Newtonian fluids.

(4) Fracture complexity is governed by the combined effects of fluid rheology and rock heterogeneity. By selecting appropriate fluids and injection rates, operators can enhance branching in viscosity-dominated fractures or mitigate instability in toughness-dominated fractures.

Acknowledgments

The authors acknowledge the support provided by the National Natural Science Foundation of China (Grant No. 52409140) and the Research Grants Council of Hong Kong, China (through GRF 16203123 and CRF C7085-24G).

Open research

The MATLAB code used for model validation in Section 3 is available in Dryad at Dontsov (2017).

Journal Pre-proof

Journal Pre-proof

References

Al-Busaidi, A., Hazzard, J.F., Young, R.P., 2005. Distinct element modeling of hydraulically fractured Lac du Bonnet granite. J. Geophys. Res. Solid Earth. 110, 1-14.

Bunger, A.P., Detournay, E., 2008. Experimental validation of the tip asymptotics for a fluid-driven crack. J. Mech. Phys. Solids. 56, 3101-3115.

Chen, Y.Q., Nagaya, Y., Ishida, T., 2015. Observations of fractures induced by hydraulic fracturing in anisotropic granite. Rock Mech. Rock Eng. 48, 1455-1461.

Chen, Z.Q., Elsworth, D., Wang, M., 2020. Does low-viscosity fracturing fluid always create complex fractures. J. Geophys. Res. Solid Earth. 125, 1-15.

Chen, Z.Q., Wang, M., 2017. Pore-scale modeling of hydromechanical coupled mechanics in hydrofracturing process. J. Geophys. Res. Solid Earth. 122, 3410-3429.

Cundall, P.A., 1971. A computer model for simulating progressive large-scale movements in blocky rock systems. In: Proceedings of the Symposium of the International Society of Rock Mechanics, Nancy, vol. 2. p. No. 8.

Detournay, E., 2016. Mechanics of hydraulic fractures. Annu. Rev. Fluid Mech. 48, 311-339.

Dontsov, E., Suarez-Rivera, R., 2021. Representation of high resolution rock properties on a coarser grid for hydraulic fracture modeling. J. Pet. Sci. Eng. 198, 108144.

Dontsov, E.V., 2017. An approximate solution for a plane strain hydraulic fracture that accounts for fracture toughness, fluid viscosity, and leak-off. Int. J. Fract. 205, 221-237.

Dontsov, E.V., 2019. Scaling laws for hydraulic fractures driven by a power-law fluid in homogeneous anisotropic rocks. Int. J. Numer. Anal. Methods Geomech. 43, 519-529.

Dontsov, E.V., Kresse, O., 2018. A semi-infinite hydraulic fracture with leak-off driven by a power-law fluid. J. Fluid Mech. 837, 210-229.

Economides, M., Nolte, K., 2000. Reservoir stimulation. Wiley, New York, NY, USA.

Fischer, T., Hainzl, S., Eisner, L., Shapiro, S.A., Le Calvez, J., 2008. Microseismic signatures of hydraulic fracture growth in sediment formations: Observations and modeling. J. Geophys. Res. Solid Earth. 113.

Garagash, D.I., 2006. Transient solution for a plane-strain fracture driven by a shear-thinning, power-law fluid. Int. J. Numer. Anal. Methods Geomech. 30, 1439-1475.

Garagash, D.I., Detournay, E., Adachi, J.I., 2011. Multiscale tip asymptotics in hydraulic fracture with leak-off. J. Fluid Mech. 669, 260-297.

Guo, T.K., Rui, Z.H., Qu, Z.Q., Qi, N., 2018. Experimental study of directional propagation of hydraulic fracture guided by multi-radial slim holes. J. Pet. Sci. Eng. 166, 592-601.

Hossain, M.Z., Hsueh, C.J., Bourdin, B., Bhattacharya, K., 2014. Effective toughness of heterogeneous media. J. Mech. Phys. Solids. 71, 15-32.

Hu, J., Garagash, D.I., 2010. Plane-strain propagation of a fluid-driven crack in a permeable rock with fracture toughness. J. Eng. Mech. 136, 1152-1166.

Huang, L.K., Liu, J.J., Zhang, F.S., Dontsov, E., Damjanac, B., 2019. Exploring the influence of rock inherent heterogeneity and grain size on hydraulic fracturing using discrete element modeling. Int. J. Solids Struct. 176-177, 207-220.

Ishida, T., Chen, Y.Q., Bennour, Z., et al., 2016. Features of CO2 fracturing deduced from acoustic emission and microscopy in laboratory experiments. J. Geophys. Res. Solid Earth. 121, 8080-8098.

Ishida, T., Sasaki, S., Matsunaga, I., Chen, Q., Mizuta, Y., 2000. Effect of grain size in granitic rocks on hydraulic fracturing mechanism. Trends Rock Mech. 128-139.

Itasca Consulting Group Inc., 2014. PFC2D-Particle flow code in 2 dimensions, version 5.0. Minneapolis, Minnesota, USA.

Kong, L., Shang, J.L., Ranjith, P.G., et al., 2024. Grain-based DEM modelling of mechanical and coupled hydro-mechanical behaviour of crystalline rocks. Eng. Geol. 107649.

Lan, H.X., Martin, C.D., Hu, B., 2010. Effect of heterogeneity of brittle rock on micromechanical extensile behavior during compression loading. J. Geophys. Res. Solid Earth. 115, 1-14.

Lecampion, B., Bunger, A.P., Zhang, X., 2018. Numerical methods for hydraulic fracture propagation: A review of recent trends. J. Nat. Gas Sci. Eng. 49, 66-83.

Journal Pre-proof

Lecampion, B., Desroches, J., 2015. Simultaneous initiation and growth of multiple radial hydraulic fractures from a horizontal wellbore. J. Mech. Phys. Solids. 82, 235-258.

Li, M.Y., Li, M.L., Zhang, F.S., Wu, Z.J., Zhou, Y., Zhang, X.F., 2025a. Assessing the contribution of mineral composition to meso-macro progressive failure in granite under thermo-hydro-mechanical (THM) conditions: Inspiration for hydraulic fracturing in Enhanced Geothermal Systems (EGS). Int. J. Rock Mech. Min. Sci. 194, 106238.

Li, M.Y., Wong, L.N.Y., Wu, Z.J., Zhang, F.S., Wang, Z.Y., 2024a. Characterizing thermo-hydro-mechanical behavior of rock using a grain interface-based discrete element model (GIB-DEM). Eng. Anal. Bound. Elem. 166, 105814.

Li, M.L., Wu, J.F., Li, J.F., Zhuang, L., Wang, S.Y., Zhang, F.S., 2022. Modeling of hydraulic fracturing in polymineralic rock with a grain-based DEM coupled with a pore network model. Eng. Fract. Mech. 275, 108801.

Li, M.Y., Wu, Z.J., Weng, L., Wu, Y., Wang, Z.Y., Liu, Q.S., 2023. Tensile strength degradations of mineral grain interfaces (MGIs) of granite after thermo-hydro-mechanical (THM) treatment. Int. J. Rock Mech. Min. Sci. 171, 105592.--

Li, M.L., Zhang, F.S., Li, M.Y., Dontsov, E., Valov, A., Wang, T., 2025b. Competitive fracture propagation across different regimes during multi-stage hydraulic fracturing. Int. J. Solids Struct. 113817.

Li, M.L., Zhang, F.S., Wang, S.Y., Dontsov, E., Li, P.C., 2024b. DEM modeling of simultaneous propagation of multiple hydraulic fractures across different regimes, from toughness to viscosity-dominated. Rock Mech. Rock Eng. 57, 481-503.

Li, M.L., Zhang, F.S., Zhuang, L., Zhang, X., Ranjith, P., 2020. Micromechanical analysis of hydraulic fracturing in the toughness-dominated regime: implications to supercritical carbon dioxide fracturing. Comput. Geosci. 24, 1815-1831.

Liu, C.X., Zhang, F.S., Detournay, E., 2025. Finite domain solution of a hydraulic fracture in a permeable rock. Rock Mech. Bull. 4, 100156.

Liu, H.Y., Roquete, M., Kou, S.Q., Lindqvist, P.A., 2004. Characterization of rock heterogeneity and numerical verification. Eng. Geol. 72, 89-119.

Liu, S., Shen, Y.X., 2025. Effective fracture toughness for heterogeneous materials accounting for the worst-case scenario. J. Mech. Phys. Solids. 106333.

Ouchi, H., Agrawal, S., Foster, J.T., Sharma, M.M., 2017. Effect of small scale heterogeneity on the growth of hydraulic fractures. In: SPE Hydraul. Fract. Technol. Conf. Exhib. SPE, D021S003R002.

Pan, X.H., Guo, W., Wu, S.F., Chu, J., 2020. An experimental approach for determination of the Weibull homogeneity index of rock or rock-like materials. Acta Geotech. 15, 375-391.

Peirce, A.P., Siebrits, E., 2005. A dual mesh multigrid preconditioner for the efficient solution of hydraulically driven fracture problems. Int. J. Numer. Methods Eng. 63, 1797-1823.

Potyondy, D.O., 2010. A grain-based model for rock: Approaching the true microstructure. Rock Mech. Nord. Ctries. 225-234.

Potyondy, D.O., Cundall, P.A., 2004. A bonded-particle model for rock. Int. J. Rock Mech. Min. Sci. 41, 1329-1364.

Rice, J.R., 1968. Mathematical analysis in the mechanics of fracture. Fracture: An Advanced Treatise. 2, 191-311.

Rivalta, E., Taisne, B., Bunger, A.P., Katz, R.F., 2015. A review of mechanical models of dike propagation: Schools of thought, results and future directions. Tectonophysics. 638, 1-42.

Tanné, E., Bourdin, B., Yoshioka, K., 2022. On the loss of symmetry in toughness dominated hydraulic fractures. Int. J. Fract. 237, 189-202.

Wang, S.F., Elsworth, D., Zhang, L.P., Zhao, X.Y., Wang, T., 2025a. Hydro-grain-texture modeling of systematics of propagation, branching, and coalescence of fluid-driven fractures. Rock Mech. Rock Eng. 58, 623-644.

Wang, S.F., Wang, T., Li, S., Tong, D.F., Chen, T.Y., 2025b. Simultaneous Propagation of Multiple Hydraulic Fractures in Crystalline Rock: A Numerical Investigation Based on Coupled Fluid-Solid Discrete Element Framework. Rock Mech. Bull. 100277.

Wang, T., Li, M.L., 2025. Particle migration and pore clogging in porous media during supercritical carbon dioxide sequestration. Comput. Geotech. 185, 107316.

Wang, T., Zhang, F.S., Furtney, J., Damjanac, B., 2022. A review of methods, applications and limitations for incorporating fluid flow in the discrete element method. J. Rock Mech. Geotech. Eng. 14, 1005-1024.

Wang, Z.Y., Li, Y.W., Wu, Z.J., 2023. Hierarchical scaling model for size effect on tensile strength of polycrystalline rock. Int. J. Mech. Sci. 247, 108171.

Wei, M.D., Dai, F., Liu, Y., Jiang, R.C., 2023. A fracture model for assessing tensile mode crack growth resistance of rocks. J. Rock Mech. Geotech. Eng. 15, 395-411.

Wei, M.D., Dai, F., Liu, Y., Li, A., Yan, Z.L., 2021. Influences of loading method and notch type on rock fracture toughness measurements: from the perspectives of T-stress and fracture process zone. Rock Mech. Rock Eng. 54, 4965-4986.

Wu, M.Y., Gao, K., Liu, J.J., Song, Z.L., Huang, X.L., 2022. Influence of rock heterogeneity on hydraulic fracturing: A parametric study using the combined finite-discrete element method. Int. J. Solids Struct. 234, 111293.

Yang, C.Y., Zhu, F., Zhao, J.D., 2024. Coupled total-and semi-Lagrangian peridynamics for modelling fluid-driven fracturing in solids. Comput. Methods Appl. Mech. Eng. 419, 116580.

Zang, A., Zimmermann, G., Hofmann, H., Stephansson, O., Min, K.B., Kim, K.Y., 2019. How to reduce fluid-injection-induced seismicity. Rock Mech. Rock Eng. 52, 475-493.

Zhang, E.Y., Wen, D.G., Wang, G.L., et al., 2024. Two stages power generation test of the hot dry rock exploration and production demonstration project in the Gonghe Basin, northeastern Qinghai-Tibet plateau, China. China Geol. 7, 409-421.

Zhang, F.S., Damjanac, B., Huang, H.Y., 2013. Coupled discrete element modeling of fluid injection into dense granular media. J. Geophys. Res. Solid Earth. 118, 2703-2722.

Zhang, F.S., Damjanac, B., Maxwell, S., 2019a. Investigating hydraulic fracturing complexity in naturally fractured rock masses using fully coupled multiscale numerical modeling. Rock Mech. Rock Eng. 52, 5137-5160.

Zhang, X., Si, G.Y., Zhang, J.G., Wang, M., Zhao, G.Z., Oh, J., 2025. Seismic Characterisation of Hydraulic Fractures Influenced By Granitic Coarse Grains. Rock Mech. Rock Eng.

Zhang, Y.H., Wong, L.N.Y., Chan, K.K., 2019b. An extended grain-based model accounting for microstructures in rock deformation. J. Geophys. Res. Solid Earth. 124, 125-148.

Zhuang, L., Jung, S.G., Diaz, M., et al., 2020. Laboratory true triaxial hydraulic fracturing of granite under six fluid injection schemes and grain-scale fracture observations. Rock Mech. Rock Eng. 53, 4329-4344.

Zhuang, L., Zang, A., 2021. Laboratory hydraulic fracturing experiments on crystalline rock for geothermal purposes. Earth Sci. Rev. 216, 103580.

Journal Pre-proof

Fengshou Zhang obtained his BSc and MSc degrees in Civil Engineering from Tongji University, China, in 2004 and 2007, respectively, and his PhD in Geotechnical Engineering from the Georgia Institute of Technology, USA, in 2012. He worked as a geomechanics engineer in Itasca Consulting Group, Inc. from 2012 to 2016. Since 2016, he joined the Department of Geotechnical Engineering at Tongji University as a professor. His research interests include: (1) Multifield coupling of rock mechanics and its application in deep earth engineering such as shale gas and dry hot rock; (2) Damage and migration mechanisms of granular materials under fluid-solid interaction; (3) Theoretical and numerical modeling analysis of the behavior of soil and rock; and (4) Carbon dioxide geological storage and energy storage.

Declaration of Interest Statement

☒ The authors declare that they have no known competing financial interests or personal relationships that could have appeared to influence the work reported in this paper.

☒ The author Fengshou Zhang is an Editorial Board Member for this journal and was not involved in the editorial review or the decision to publish this article.

☐ The authors declare the following financial interests/personal relationships which may be considered as potential competing interests:

Journal Pre-proof